Tellus
SERIES B
CHEMICAL
AND PHYSICAL
METEOROLOGY
PUBLISHED BY THE INTERNATIONAL METEOROLOGICAL INSTITUTE IN STOCKHOLM

Tellus (2011), 63B, 573–588
Printed in Singapore. All rights reserved

TELLUS

Spectral particle absorption coefficients, single scattering albedos and imaginary parts of refractive indices from ground based in situ measurements at Cape Verde Island during SAMUM-2

By T. MÜLLER[1,*], A. SCHLADITZ[1], K. KANDLER[2] and A. WIEDENSOHLER[1], [1]*Leibniz Institute for Tropospheric Reseach, Permoserstraße 15, 04318 Leipzig, Germany;* [2]*Institut für Angewandte Geowissenschaften, Technische Universität Darmstadt, Schnittspahnstraße 9, 64287 Darmstadt, Germany*

(Manuscript received 20 December 2010; in final form 9 June 2011)

ABSTRACT

During the SAMUM-2 experiment, spectral absorption coefficients, single scattering albedos and imaginary parts of refractive indices of mineral dust particles were investigated at the Cape Verde Islands. Main absorbing constituents of airborne samples were mineral dust and soot. PM_{10} spectral absorption coefficients were measured using a Spectral Optical Absorption Photometer (SOAP) covering the wavelength range from 300 to 960 nm with a resolution of 25 nm. From SOAP, also information on the particle scattering coefficients could be retrieved. Spectral single scattering albedos were obtained in the wavelength range from 350 to 960 nm. Imaginary parts of the refractive index were inferred from measured particle number size distributions and absorption coefficients using Mie scattering theory. Imaginary parts for a dust case were 0.012, 0.0047 and 0.0019 at the wavelengths 450, 550 and 950 nm, respectively, and the single scattering albedos were 0.91, 0.96 and 0.98 at the same wavelengths. During a marine case, the imaginary parts of the refractive indices were 0.0045, 0.0040 and 0.0036 and single scattering albedos were 0.93, 0.95 and 0.96 at the wavelengths given above.

1. Introduction

Mineral dust is an important constituent of airborne particles and affects the Earth's climate system (Haywood and Bougher, 2000; IPCC, 2007). It is thus essential to understand the processes of formation, transport and modification of the mineral dust aerosol. Dust sources are distributed all over the globe (Prospero et al., 2002). Mineral dust from the Saharan desert may travel thousands of kilometres across the Atlantic Ocean (Kaufman et al., 2005).

Radiative forcing by mineral dust particles is complex, since dust particles scatter and partly absorb incoming solar radiation. They also absorb and emit outgoing long-wave radiation depending on mineralogical composition and wavelength. Besides the composition, the quantity of the dust-induced radiative forcing also depends on the mass and particle size of suspended dust, the vertical distribution and the albedo of the underlying surface (Sokolik and Toon, 1996; Tegen et al., 1996).

The strength of interaction between particles and radiation can be given by the absorption and scattering coefficients. These parameters are also observables by in situ aerosol measurements. Scattering and absorption depend on the chemical and mineralogical composition, the size and the shape of mineral dust particles. During transport, the size as well as the composition and thus absorption and scattering may change. The interaction of particles with radiation emerges from a more fundamental parameter, the complex refractive index. However, refractive indices cannot be measured directly. The complex refractive index reflects the chemical and mineralogical composition. Using the scattering theory, modellers derive the impact of mineral dust on the Earth's radiation budget and also the feedback mechanism on the dust mobilization (e.g. Heinold et al., 2008). As shown by Sokolik and Toon (1999), the imaginary part of the refractive index of mineral dust is strongly variable in the spectral range from the ultraviolet (UV) to the near infrared (NIR). Therefore, the investigation of spectral optical properties is of special interest and is needed to understand the impact of the mineral dust aerosol. The lack of spectral refractive indices for dust particles, mixed with other compounds, for example, sea salt, sulphate, soot and biomass burning smoke, is a weak point

---

[*] Corresponding author.
e-mail: thomas.mueller@tropos.de
DOI: 10.1111/j.1600-0889.2011.00572.x

in modelling the impact of mineral dust on the Earth's radiation budget.

Complex refractive indices might be derived by measuring the chemical/mineralogical composition or by determining microphysical parameters as particle number size distribution and shape of particles and measuring the particle absorption and scattering coefficients. An overview of refractive indices of mineral dust is given for instance in Sokolik and Toon (1999). In the recent years, optical dust properties were investigated in laboratory studies (e.g. Linke et al., 2006) and measured during field experiments (e.g. Haywood et al., 2001; Haywood et al., 2003). The SAMUM-1 experiment (Heintzenberg, 2009) held in southern Morocco was a dust closure experiment in a source region with a minimum impact of maritime, anthropogenic and biogenic aerosol sources. Refractive indices were delivered by Müller et al. (2009a), Schladitz et al. (2009) and Kandler et al. (2009).

Whereas measurements of the absorption coefficients at few discrete wavelengths are a first estimate of quantifying the total absorption of suspended dust, a differentiation between the major absorbing compounds, for example, mineral dust, smoke and soot, is difficult. Measurements of the absorption coefficient at multiple wavelengths for determination of dust were done with the aethalometer (Coen et al., 2004; Fialho et al., 2006) and the Particle Soot Absorption Photometer (PSAP, e.g. Petzold et al. 2009). A spectral optical absorption photometer (SOAP) was first employed during the intense field study SAMUM-1 to measure the absorption coefficient from 300 to 950 nm. All these instruments suffer from a cross sensitivity to particle scattering. Corrections for the cross sensitivity are discussed in Section 3.4.2.

Field campaigns are important to validate atmospheric models (Heinold et al., 2009; Müller et al., 2009b) as well as satellite remote sensing retrievals (Kahn et al., 2009), since optical parameters derived from model calculations rely on particle number size distributions and refractive indices. Introductions and summaries of key findings to the field campaigns SAMUM-1 and SAMUM-2 are given in Heintzenberg (2009) and Ansmann et al. (2011). A description of the measurement site of SAMUM-2 is given in Section 2. In Section 3, the instrumentation used for measuring the particle number size distribution and scattering and absorption coefficients is introduced. Aerosol parameters often used to describe the optical properties are given in Section 4. Measurements of aerosol parameters and derived imaginary parts of refractive indices are given in Section 5, followed by a comparison of refractive indices derived from the SAMUM-1 and SAMUM-2 campaigns.

2. Measurement site

The Saharan mineral dust experiment SAMUM-2 was conducted at Cape Verde Islands from January to February 2008. A field station with in situ ground observations and remote sensing techniques (aerosol LIDAR, wind LIDAR and sun photometer) was setup at the airport of Praia (14°57′N, 23°29′W) in the southeast of the Island Santiago. Furthermore the research aircraft Falcon 20-E of the German Aerospace Center (DLR) was stationed at Praia airport. Onboard of the research aircraft particle number size distributions and absorption coefficients were measured. The field station was located about 2 km west of the coastline. For an overview of the measurement site and the surrounding area we refer to Kandler et al. (2011b) and Schladitz et al. (2011b). The next largest city Praia with about 100.000 inhabitants is 3 km southwest of the station. Because of the continuous trade winds from the Northeast, contamination due the city of Praia did not occur. No anthropogenic pollution of nearby sources was expected when the wind was from the east, since there were neither villages nor other islands. There was a small village in the northeast sector in a distance of about 1 km, and the Island Maio in a distance of 35 km. However, we expected no significant pollution by local emissions, since there were only little traffic and houses typically have no heating.

3. Instrumentation

3.1. *Aerosol inlet and particle losses*

In situ measurements of microphysical and optical particle properties were performed in an air-conditioned container with temperatures of approximately 20 °C. A suite of instruments was placed inside and on top of the container. Only a part of these instruments is however used for this study.

The aerosol inlet system was mounted on the roof of the container. The outer part of the inlet systems consists of a PM_{10} inlet (50% transmission efficiency at 10 μm aerodynamic diameter) in a height of about 6 m above ground. Downstream of the PM_{10} inlet, an automatic aerosol diffusion dryer (Tuch et al., 2009) was installed to ensure an aerosol humidity smaller than 30% to prevent hygroscopic particle growth. Inside of the container, the aerosol stream was split isokinetically into several aerosol flows and particles were directed to the instruments. The most severe mechanism for particle losses was gravitational settling and impaction of coarse mode particles larger than 1 μm in horizontal lines and bends, respectively. To minimize particle losses, the instruments for measuring physical properties of coarse mode particles were placed close to the inlet and sampling lines were kept as short as possible. We tried to avoid horizontal sampling lines. Remaining particle losses were accounted for using formulas given in Brockmann (1993).

Instruments necessary to derive spectral absorption, refractive index and single scattering albedo were absorption photometers, particle size spectrometers and an integrating nephelometer for measuring the particle scattering coefficient. The set of instruments is described in the following sections.

3.2. *Particle number size distribution*

Particle number size distributions were measured with a Differential Mobility Particle Sizer (DMPS; e.g. Birmili et al., 1999) with a range of mobility diameters from 26 to 800 nm. An Aerodynamic Particle Sizer (APS; model 3321, TSI Inc., St. Paul, USA) was used for measuring particle number size distributions from 0.8 to 10 μm in aerodynamic diameter. Particles relevant for optical properties are found in the fine and coarse mode range. The APS was placed directly below the aerosol inlet to avoid losses by impaction and sedimentation, which would largely affect the particle volume size distribution. Particle transport losses to the DMPS can be neglected, since losses by sedimentation and impaction are negligible for the size range of the DMPS.

Particle size spectra measured with DMPS are affected by multiple charged particles. An inversion algorithm was applied to correct for the multiple charge effects. However, inversion routines are constrained to conditions where the number concentration of particles larger than the largest diameter channel of the DMPS is negligible. For aerosols with a large number concentration of coarse mode particles, for example, sea salt or mineral dust, this constrained is not fulfilled. Instead, the aerodynamic number distribution measured with APS is used to simulate multiple charge effects in the mobility spectrum of DMPS. During SAMUM-1, with a large number concentration of coarse mode particles, the overlap between largest DMPS diameters and smallest APS diameters was a crucial point. A detailed description of the algorithm for considering multiple charge effects in the APS size range, inversion of DMPS spectra and combining inverted DMPS and APS spectra is given in Schladitz et al. (2009). The performance of this algorithm to improve the overlap between DMPS and APS is shown in Birmili et al. (2008) for a strong dust event over Europe.

It has to be considered that electrical mobility and aerodynamic diameters are connected by the particle density and dynamical shape factor, and both diameters were converted to volume equivalent diameters (DeCarlo et al., 2004). For the present measurements, particle density and dynamic shape factors differ between sea salt and mineral dust, which are the prevailing aerosol types in the coarse mode. In the APS size range, dynamic shape factors of 1.08 and 1.25 for sea salt and for Saharan mineral dust particles were used, and the particle density was 2160 kg m^{-3} for sea salt and 2600 kg m^{-3} for mineral dust particles, respectively (Schladitz et al., 2011a). In the DMPS size range, particles are assumed to be ‘spherical’ and thus the dynamical shape factor equals unity.

3.3. *Particle scattering coefficients*

Particle scattering and hemispheric backscattering coefficients were measured with an integrating nephelometer (model 3563, TSI Inc., St. Paul, USA) at wavelengths of 450, 550 and 700 nm. Values measured with nephelometers are affected by two systematic errors. These are a limited angular integration range from 7° to 170° and a non-Lambertian intensity distribution of the light source. For details, the reader is referred to e.g., Anderson et al. (1996). Both, the limited angular range and the intensity function of the nephelometer (TSI model 3563) are known (Anderson et al., 1996; Müller et al., 2009c) and correction factors can be estimated using Mie calculations (e.g. Heintzenberg et al., 2006) to account for the systematic errors. Mie calculations require particle number size distributions and refractive indices. Schladitz et al. (2011b) showed in a closure study that scattering coefficients inferred by Mie calculation underestimate the measured scattering coefficient by far in presence of mineral dust. For example, the measured scattering coefficients at 550 nm wavelength are about 60% higher than calculated values.

For cases with low mineral dust concentrations, measured and calculated scattering coefficients agreed well. To our best knowledge, there is presently no published study on the error of nephelometer corrections in presence of non-spherical particles. Another correction, we used for our analysis, was given by Anderson and Ogren (1998). The correction is based on scattering Ångström exponents, which is a measure of wavelength dependence of scattering coefficients, measured by the nephelometer itself. Parameterizations to correct the total scattering are given as function of scattering Ångström exponents, which were derived from uncorrected values of measured scattering coefficients. For the SAMUM-2 campaign, this approach led to correction factors between 1.43 and 1.23 at a wavelength of 450 nm. Correction factors at the wavelength 550 nm are between 1.35 and 1.22, and at a wavelength of 700 nm the values for corrections factors are between 1.29 and 1.19. The higher values of correction factors correspond to cases with high concentrations of mineral dust, and the lower values correspond to a dust free period. It is noted in Anderson and Ogren (1998), that the uncertainty of this correction might be high since the correction factor is not well constrained to the Ångström exponent for super-micron particles. Anderson and Ogren (1998) also pointed out that the correction factors arises mostly due to forward scattering, which is insensitive to shape effects (Mishchenko et al., 1995). For that reason and a lack of a detailed error analysis of the nephelometer corrections including shape effects, we have taken the highest uncertainty given in Anderson and Ogren (1998), which amounts of about ±22%. Including an additional uncertainty of about ±3% from the calibration of nephelometers (Müller et al., 2009c; Anderson et al., 1996), we estimated the total uncertainty of the scattering coefficients to be ±25% in case of high mineral dust concentrations.

3.4. *Spectral optical absorption photometer (SOAP)*

3.4.1. Instrument description. The SOAP was introduced in Müller et al. (2009a). Beside technical modifications, also the data evaluation was improved to retrieve absorption coefficients. Additionally to the particle absorption, also information on the particle scattering was derived from SOAP.

The SOAP measures the transmittance and reflectance of fibre filters (Pallflex E70/2075W) while particles are collected on the filter. The light source is a deuterium lamp with emission from the ultraviolet to NIR spectral range. In the original instrument, the reflected and transmitted spectral radiance is measured with an optical spectrophotometer, which covers the spectral range from 200 to 800 nm with an optical resolution of 50 nm. With a mechanical switch the spectral photometer is coupled either to the reflection or the transmission channel, what allows to measure transmittance and reflectance with a single spectrophotometer. The measured transmittance τ and reflectance ρ are functions of the particle absorption and scattering optical depths. The particle optical depths are defined by $OD_x = \sigma_x\ Q\ \Delta t/A$, where σ_x is either the absorption or scattering coefficient, Q is the aerosol flow rate, Δt is the total sampling time and A is the spot size area of the sample. In Müller et al. (2009a), absorption coefficients were derived by solving the radiative transfer problem with pre-calculated lookup tables, which were generated by a ray tracing model.

3.4.2. Improvements of performance and recalibration. The instrument performance was improved by replacing the mechanical switch and the single spectrophotometer by two spectrophotometers, one for transmittance and reflectance measurements, respectively. The spectral ranges of the new spectrophotometers are from 200 to 960 nm with an optical resolution of 25 nm. The full spectral range cannot be used, because of a too low signal to noise ratio for wavelengths smaller 300 nm.

Beside the technical improvements also the data processing was changed. The pre-calculated lookup-tables were replaced by a two-stream radiative transfer model. The radiative transfer model was adopted from Bohren (1987) and Arnott et al. (2005). Input parameters for both models are the scattering and the absorbing optical depth of the filter, the asymmetry parameter for filter and particle scattering, and the particle penetration depth. The input parameters for the two-stream model are the same as used for the ray-tracing approach. The ray-tracing model also included calibration factors, which were derived from experiments with non-absorbing and strongly absorbing particles. New calibration experiments (Meusinger 2009) revealed that the calibration can be improved by using loading-dependent calibration functions. The new and the old data retrieval were compared with a test data set. Differences in the absorption coefficients were less than 8%. For a time resolution of 10 min, the detection limits of SOAP are approximately 0.25 and 0.5 Mm^{-1} for wavelengths larger and smaller 450 nm, respectively.

In Müller et al. (2009a), the uncertainty of retrieved absorption coefficients was determined to be 15%. Since no independent reference for measuring absorption coefficients was available, the uncertainty is also assumed to be 15% for the modified absorption photometer. Filter based absorption photometers suffer from a cross sensitivity to particle scattering. In Bond et al. (1999) and Müller et al. (2011), a cross sensitivity to particle scattering of about 1.6% ± 1.6% was found for the Particle Soot Absorption Photometer (PSAP, Radiance Research, Seattle, WA, USA). This means that 1.6% of the scattering coefficient are seen by the instrument as an apparent absorption. Since SOAP and PSAP are similar in the design of the measuring head and use the same type of filter (Pallflex E70/2075W), scattering artefacts also affect measurements done with SOAP. For PSAP the cross sensitivity to scattering is accounted for by subtracting about 1.6% of the measured scattering coefficients (Bond et al. 1999). The SOAP corrects internally for scattering by use of an additional reflectance measurement. With laboratory measurements it was shown that the data retrieval of SOAP corrects for apparent absorption, but with a remaining uncertainty of 2% of the scattering coefficients. This means that the uncertainty of the scattering correction is as high as the correction itself. The total uncertainty of absorption coefficients derived from SOAP consists of two parts and can be written as $\Delta\sigma_{\mathrm{abs}} = \pm(0.15\ \sigma_{\mathrm{abs}} + 0.02\ \sigma_{\mathrm{sca}})$.

3.4.3. Derivation of spectral scattering coefficients from the SOAP. From the two-stream method, we concluded that also the particle scattering coefficient can be inferred, when measuring transmittance and reflectance (cf. eqs 17 and 18 in Arnott et al. 2005). The two-stream method also requires the particle asymmetry parameter. Asymmetry parameters were calculated using the Mie theory. Refractive indices for this calculation were taken from the SAMUM-1 campaign (Müller et al. 2009a). 10th and 90th percentiles for the distribution of asymmetry parameter were 0.71 and 0.78 at 450 nm, and 0.66 and 0.71 at 800 nm, respectively. Since this parameter cannot be derived from SOAP, a test data set was used to test the sensitivity on the particle asymmetry parameter in the range from 0.66 to 0.78. It was found that the sensitivity to the particle asymmetry parameter is less than 1% when deriving particle absorption coefficient. In contrast, derived scattering coefficients vary as much as ±30%. Data of the SAMUM-2 campaign were evaluated with a constant asymmetry parameter of 0.71. This value is the median of the distribution of asymmetry parameters for the entire campaign at wavelength 550 nm. The uncertainty of the scattering is given by the variation of scattering coefficients and amounts ±30%.

Uncorrected scattering coefficients from the SOAP are plotted versus the scattering coefficients determined from nephelometer at wavelengths 450, 550 and 700 nm (cf. Fig. 1). Scattering coefficients measured with SOAP are smaller than scattering coefficients measured with nephelometer, but correlation coefficients (r) were found to be between 0.95 and 0.98. The correlations coefficients are relatively high, although the uncertainty due the assumption of a constant asymmetry is up to ±30%. We believe that the correlation coefficients are affected by the signal-to-noise ratio of the SOAP. The signal to noise ratio of nephelometer is much better compared to that of SOAP. Slopes of regression lines for the wavelengths 450, 550 and 700 nm were found to be 0.66, 0.60 and 0.56. The intercept values for all three wavelengths were between –5.5 and 0.6 Mm^{-1} and were neglected. For deriving a calibration for the SOAP, the slopes of

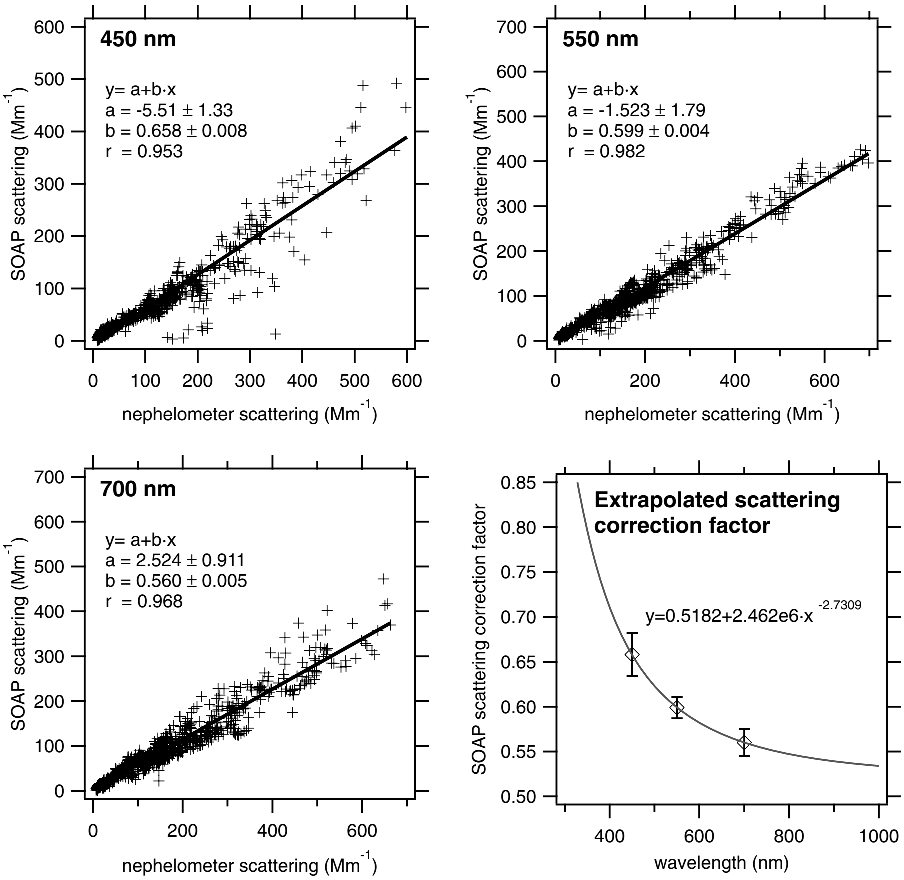

Fig. 1. Linear regression of scattering coefficients measured with SOAP and nephelometer at 450, 550 and 700 nm. Lower right panel: Extrapolation of scattering correction factors to 300 nm and 1000 nm. The error bars are the uncertainties of the slopes with 99% confidence level.

the regression lines were plotted versus the wavelength (Fig. 1, lower right panel). It was found that a power law plus an additional bias yields a best fit to measured data. There is a severe dependence of the correction on the wavelength. The reason for the spectral dependence is not clear till now. However, the fit function was used to extrapolate correction factors in the wavelength range between 300 and 950 nm.

Scattering coefficients calculated from SOAP are subject to uncertainties of the fit-function and to uncertainties of the scattering measured with nephelometer. The uncertainty of the fitted data (slopes) in the fit function is about 4% with a confidence level of 99%. The uncertainty of scattering coefficients from nephelometer was estimated to about 25% (cf. Section 3.3). Error propagation yields a total uncertainty of the SOAP derived scattering coefficient of 41%, 35%, 32%, 30% and 29% at wavelengths 300, 400, 500, 700 and 900 nm, respectively.

4. Methods

Beside the instrument specific correction, all data presented in this manuscript were adjusted to STP (Standard Temperature and Pressure, $T_0 = 0$ °C and $P_0 = 1013.25$ hPa) conditions. Scattering and absorption coefficients measured at temperature T and pressure P were multiplied by the factor $(T_0 P)\big/(T P_0)$ and resulting values referred to STP conditions. Dates and times are given as Day of the Year (DOY; e.g., DOY 1.5 equals 1 January, 12:00) throughout the manuscript.

For the following consideration, it should keep in mind, that all instruments were placed downstream of a PM_{10} inlet. Extensive quantities (value of the quantity depends on the amount of material, e.g. concentrations, scattering and absorption coefficients) are affected by the size cut. Derived intensive quantities (value independent on amount of material, single scattering albedo and refractive index) of coarse mode particles are expected not to be affected by the size cut, since the chemical composition of coarse mode particles is assumed to be nearly size-independent (Kandler et al. 2011a). In contrast, intensive properties of the entire particle population (sub-micrometer plus coarse mode particles) could be affected by the size cut, since the ratio of volume concentrations of sub-micrometer and super-micrometer size fractions strongly depends on the cut-off diameter.

Typically refractive indices were derived by inverse Mie calculations assuming spherical particles. In Schladitz et al.

(2011b), it was shown that scattering coefficients derived from Mie-theory underestimate measured particle scattering coefficients by a factor of about 1.6 at the wavelength 550 nm. In contrast, the particle absorption is less sensitive to the particle shape. Therefore, it is valid to derive imaginary parts of refractive indices by inverse Mie calculations using measured particle number size distributions and measured particle absorption coefficients. Details are given in Section 5.3.

The absorption and scattering Ångström exponents (α_{abs} and α_{sca}) are defined by

$$\alpha_{\text{abs}}(\lambda_1, \lambda_2) = -\ln(\sigma_{\text{abs}}(\lambda_1)/\sigma_{\text{abs}}(\lambda_2)) / \ln(\lambda_1/\lambda_2) \tag{1}$$

and

$$\alpha_{\text{sca}}(\lambda_1, \lambda_2) = -\ln(\sigma_{\text{sca}}(\lambda_1)/\sigma_{\text{sca}}(\lambda_2)) / \ln(\lambda_1/\lambda_2)\,. \tag{2}$$

Eqs 1 and 2 are adopted from the original definition of extinction Ångström exponents (Ångström, 1929). Ångström exponents are a measure of the spectral dependence within the wavelength interval λ_1 to λ_2. From the SOAP absorption, Ångström exponents at different wavelength pairs were calculated. Scattering Ångström exponents were derived from nephelometer, since scattering coefficients from the SOAP are much noisier compared to the nephelometer. We are thus limited to the three nephelometer wavelengths and to two scattering Ångström exponents, which are $\alpha_{\text{sca}}(450, 550)$ and $\alpha_{\text{sca}}(550, 700)$.

The single scattering albedo defined by

$$\omega_0 = \sigma_{\text{sca}} / (\sigma_{\text{sca}} + \sigma_{\text{abs}}) \tag{3}$$

is one of the main parameters determining the climatic effect of the atmospheric aerosol (Heintzenberg et al., 1997). Single scattering albedos were derived for wavelengths between 300 and 950 nm from the SOAP.

The uncertainty of the single scattering albedo $\Delta\omega_0$ is determined by error propagation of eq. 3 and the uncertainties of measured particle scattering and absorption coefficients. Uncertainties in the scattering coefficients were determined to between 41% and 29%. For simplicity, error calculations were done for the worst-case uncertainty of 41%. The uncertainty of the absorption coefficient consist of a measurement uncertainty of 15% and a cross sensitivity to particle scattering which amount 2% of the scattering coefficient. The resulting uncertainties at different single scattering albedos ($\omega_0 \pm \Delta\omega_0$) are 0.70 ± 0.09, 0.80 ± 0.08, 0.90 ± 0.05, 0.95 ± 0.3 and 1.0 ± 0.02. Uncertainties are little smaller when using scattering coefficients from the nephelometer. There are no systematic differences between these two single scattering albedos, since the SOAP-scattering was calibrated using the nephelometer scattering. The single scattering albedo derived from nephelometer is available only for three wavelengths, but the noise is smaller compared to single scattering albedos derived from the SOAP.

The effective radius R_{eff} is a key parameter to describe the particle number size distribution n(r). The effective radius is defined by

$$R_{\text{eff}} = \frac{\int r^3 n(r)\, \mathrm{d}r}{\int r^2 n(r)\, \mathrm{d}r}. \tag{4}$$

The effective diameter is a useful parameter to characterize the size of the entire particle population with a single parameter.

5. Results

5.1. Measured optical and microphysical properties

Figure 2 gives an overview of Ångström exponents, single scattering albedos and effective radii for the entire campaign. Absorption Ångström exponents from DOY 18 to 33 ranged between 2.24 and 4.53. The highest values of $\alpha_{\text{abs}}(450, 700)$ smaller than absorption Ångström exponents measured during SAMUM-1. During SAMUM-1 values were determined to be between 3.65 and 6.51 for mineral dust particles near ground (Müller et al., 2009a) and up to 7.0 on-board of the research aircraft Falcon (Petzold et al., 2009). After DOY 33, the dust concentration and thus also absorption Ångström exponent decreased. Between DOY 35 and 40, $\alpha_{\text{abs}}(450, 700)$ was mostly between 1.3 and 1.1. Values near unity are typical for freshly emitted soot particles (Kirchstetter et al., 2004). After DOY 40, absorption coefficients were below the detection limit of the instrument and measurements of Ångström exponents were too noise to derive reliable information on the spectral behaviour of the absorption.

Scattering Ångström exponents were smaller than unity for the entire period of the campaign. These low values indicate that the particle scattering was strongly influenced by coarse mode particles such as mineral dust or sea salt (Schladitz et al., 2011a,b). During the first period from DOY 18 to 34, the scattering Ångström exponents $\alpha_{\text{sca}}(550, 700)$ and $\alpha_{\text{sca}}(450, 550)$ ranged from −0.4 to −0.09 and −0.05 to 0.2, respectively. From DOY 33 to 37, $\alpha_{\text{sca}}(450, 550)$ increased slightly, while $\alpha_{\text{sca}}(500, 700)$ remain nearly constant. After DOY 37, both scattering Ångström exponents were almost equal and increased to about 0.75.

Time series of single scattering albedos, derived from the nephelometer and the SOAP, for the wavelengths 450, 550 and 700 nm are shown in the middle plot of Fig. 2. From DOY 18 to 35, when the absorption Ångström exponent was highest, the single scattering albedo of about 0.88 at 450 nm was significantly lower than the single scattering albedo of about 0.96 at 700 nm. With lower absorption Ångström exponents (DOY 35 to 40), the differences in the single scattering albedos at 450 and 700 nm became smaller. The average and difference of single scattering albedos at wavelengths 450 and 700 are 0.92 (avg.) and 0.1 (diff.) for period DOY 19 to 35. For the following two days (DOY

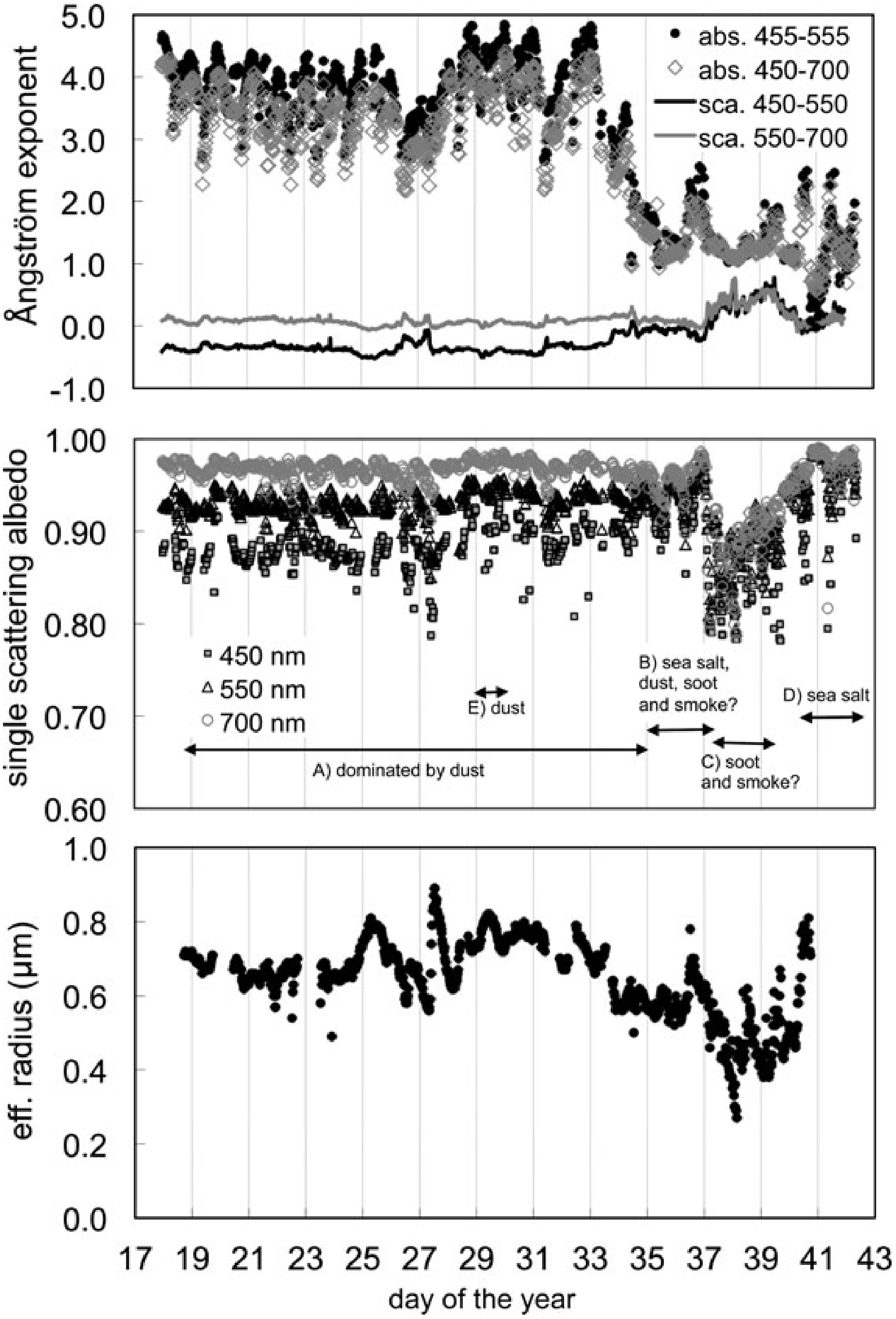

Fig. 2. Upper plot: Absorption and scattering Ångström exponents at different wavelength pairs over the entire campaign. Middle plot: Single scattering albedos for three wavelengths. Also shown is a classification of aerosol types, which is explained in more detail in Section 5.2. Lower plot: Effective radius derived from measured particle number size distributions.

35 to 37), the averages and differences are 0.93 (avg.) and 0.03 (diff.). At DOY 37, an abrupt drop in the single scattering albedo from 0.97 to 0.8 occurred and the values for both scattering Ångström exponents increased and became equal. Reasons for the change in single scattering albedos and absorption Ångström exponents were an increased mass fraction of absorbing material such as soot or possibly biomass burning smoke. A change in particle number size distribution can be seen in the effective radius. Before DOY 37, the effective radius was larger than 0.5 μm and from DOY 37 to 40, the effective radius was between 0.29 and 0.67. Small relative radii indicate that the number size distribution shifted towards smaller particles. This shift can be

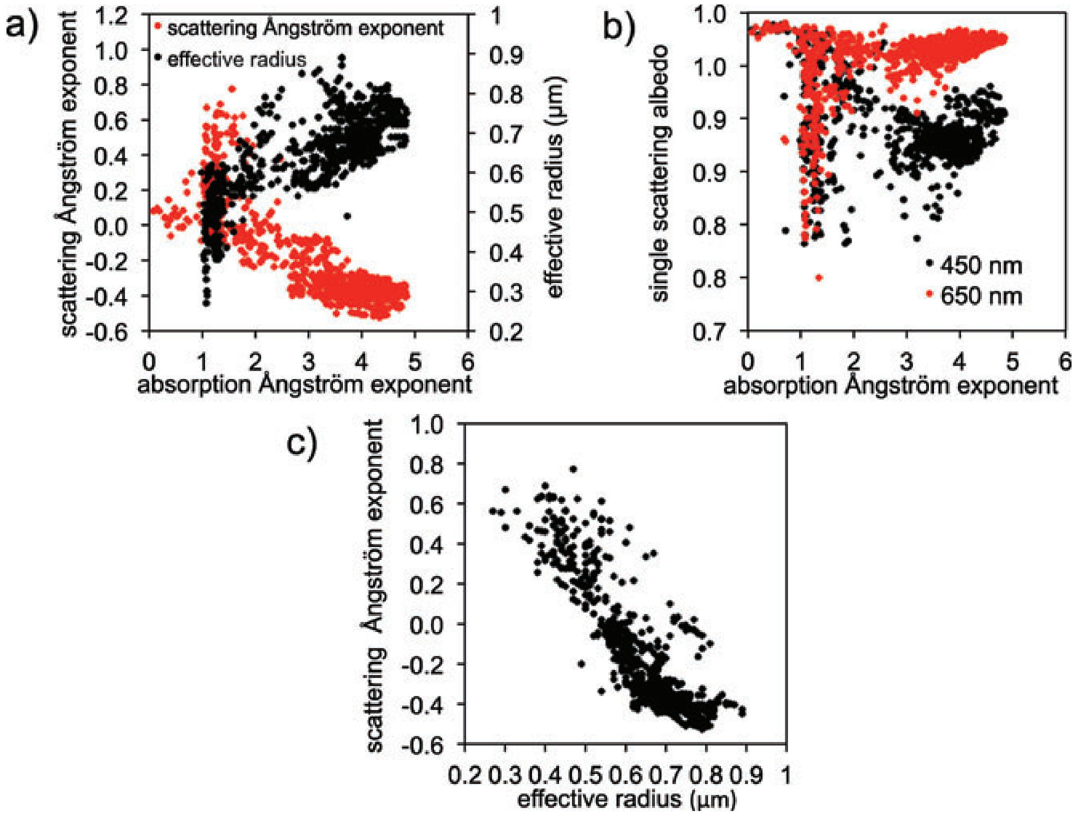

Fig. 3. (a) Scattering Ångström exponents (450–550 nm) and effective radii versus absorption Ångström exponents (450–550 nm). (b) Single scattering albedo at 450 and 650 nm versus absorption Ångström exponent (450–550 nm). (c) Correlation between scattering Ångström exponent (450–550 nm) and effective radius.

caused by either a smaller fraction of coarse mode particles, for example, dust or sea salt, or a higher fraction of accumulation mode particles, for example, marine, smoke or anthropogenic pollution.

Spectral single scattering albedos derived from the SOAP were compared to columnar integrated spectral single scattering albedos in Toledano et al. (2011) for a day with high dust concentrations near ground. Differences in single scattering albedo are smaller than 0.02 in the wavelength range between 450 and 1000 nm. In situ measured single scattering albedos refer to dry conditions, whereas data from sun photometer are measured at ambient conditions. Schladitz et al. (2011a) showed that the single scattering albedo is less sensitive to humidity effects for mineral dust particles. This insensitivity can explain the good agreement between values derived from ground-based in situ and columnar integrated measurements.

Figure 3a shows a correlation of intensive optical properties. For absorption Ångström exponents larger than two, the scattering Ångström exponent decreases with increasing absorption Ångström exponents. In this case, optical properties are dominated by mineral dust. For absorption Ångström exponents smaller than 2, the correlation became worse. Then, the absorption Ångström exponent is dominated by soot or biomass burning smoke and the scattering Ångström exponent is controlled by the relative abundance of sea salt. The effective radius shows an opposite behaviour compared to the scattering Ångström exponents. A correlation between effective radius and scattering Ångström exponent is shown in Fig. 3c. This plot indicates that the scattering Ångström exponents mainly depend on the size of particles and are not a function of the particle composition. The reader should remind that different size ranges might consist of different particle composition. That cannot be seen from Fig. 3c, since total scattering coefficients and Ångström exponents can not be used to differentiate between the dominating particle compounds, here sea-salt and mineral dust. No correlation could be found between single scattering albedos and absorption Ångström exponents (Fig. 3b). The reason is that the single scattering albedo depends on the abundance of sea salt, mineral dust and soot, whereas the absorption Ångström exponents are insensitive to sea salt.

5.2. *Aerosol type classification*

Based on the measured optical and microphysical properties, a classification of aerosol types was derived. The guidelines for classification are as follows:

(1) Sea salt mainly occurs in the coarse mode and a high mass fraction of sea salt increases the effective radius, followed by a decrease of the scattering Ångström exponent. The imaginary part of the refractive index in the wavelength range from 350 to 900 nm is smaller than 4×10^{-5} (Hess et al., 1998), since the sea salt particles are almost non-absorbing. The absorption Ångström exponent is therefore not sensitive to the mass fraction of sea salt particles.

(2) Mineral dust particles are predominantly found in the coarse mode. High mass concentrations of mineral dust cause thus high effective radii and low scattering Ångström exponents. The spectral behaviour of the imaginary part of refractive index (Müller et al., 2009a) causes high absorption Ångström exponents.

(3) Biomass burning particles (smoke) of anthropogenic and natural origin are found in the submicrometer size with small effective diameters and higher scattering Ångström exponents compared to mineral dust and sea salt. Kirchstetter et al. (2004) found absorption Ångström exponents of up to 2.5 for biomass burning aerosols. Absorption Ångström exponents at different wavelength pairs are almost constant in the wavelength range from 350 to 1000 nm.

(4) The marine background aerosol consists of aged particles of different sources. It is not possible to simply quantify the mass fraction of different compounds of aerosols by its optical properties. However, soot can be found even at remote areas (e.g. Posfai et al., 1999). Soot typically is found in the submicrometer range and values of the absorption Ångström exponents are about unity.

The definitions given in items (1) to (4) do not allow developing a strictly mathematical algorithm to classify aerosol types. The classification is not to give an insight in the mass fractions of different compounds, but to reflect concise optical properties of aerosols. Using the guidelines, five periods were indentified.

Period A: From DOY 18 to 35, the absorption Ångström exponents indicate a large mass fraction of mineral dust. The dominance of coarse mode particles can also be seen by the low scattering Ångström exponents supported by the high effective radius.

Period B: A period with a high number fraction of hygroscopic sea salt particle was observed between DOY 35 and 37.25 (Schladitz et al., 2011a). The concise optical property for this period was the high single scattering albedo at all wavelengths. A small wavelength dependence of the single scattering albedo and an absorption Ångström exponent between $\sim$1 and $\sim$2.5 might be caused in this case by different absorbing particles such as soot, biomass burning smoke, or mineral dust. The effective radius was smaller compared to the dust-dominated period. However, during the last hours of this period (DOY 36.5 to 37), we observed high single scattering albedos, increase in the absorption Ångström exponents, and a larger effective radius. The aerosol composition during this period of 12 hours is not entirely clear. From data we have, Period B can be classified as a complex mixture of several compounds of sea salt, mineral dust, biomass burning smoke and soot.

Period C: From DOY 37.25 to 39.5, scattering Ångström exponents are highest what indicates a large number fraction of small particles. For a short time period from DOY 38.5 to 39.5, the effective diameter increased, but the scattering Ångström exponent was rather constant. The absorption Ångström exponents did not change at DOY 38.5 but increased slightly at DOY 39.5. This behaviour of the optical and microphysical properties cannot be explained with the guidelines (1) to (4). Since the single scattering albedo was relatively low with values of about 0.9 or smaller, this period is classified as a mixture of soot and biomass burning smoke, although a significant amount of sea salt might have been present.

Period D: From DOY 40.5 to 42.25 was similar to period C but with a higher mass fraction of sea salt leading to a single scattering albedo larger than 0.9. The mass concentrations during this period were rather low. Scattering coefficients at all three wavelengths of the nephelometer were between 6 and 12 Mm^{-1} and absorption coefficients at 522 nm measured with a PSAP were between 0.1 and 0.5 Mm^{-1} (Schladitz et al. 2011b).

Period E: From DOY 29 to 30 is a subset of period A. During this period, the PM_{10} mass concentrations were highest with values between 430 and 520 μg/m^3 (Schladitz et al., 2011a). Since the absorption was highest with approximately 30 Mm^{-1} at a wavelength of 550 nm, this period was classified as period with the highest mineral dust mass concentration.

Figure 4 shows average spectral single scattering albedos according to the classification. Dashed lines represent the 25th and 75th percentiles. It can be seen that single scattering albedos are nearly constant for wavelengths between 650 and 950 nm. The most information on aerosol types can be found in the spectral range between 350 and 650 nm. Considering the 25th and 75th percentiles, spectral single scattering albedo allows a differentiation between the main aerosol types at the Cape Verde Islands.

The classification was compared with results from mineralogical single particle analysis (cf. fig. 8 in Kandler et al., 2011a). It was found that the time series of the relative abundance of the sum of silicate and sea salt agrees well with periods dominated by dust (periods A and E) and with periods dominated by sea salt (period B). In Knippertz et al. (2011), a classification based on back trajectories was developed. Main results of Knippertz et al. (2011) are: (i) Period A of this study was divided in three periods of dust, but with dust of different origins. (ii) The period from DOY 37 to 45 was classified by Knippertz et al. (2011) as ‘no pure dust’. (iii) Smoke layers were present at most days but layers usually occurred in heights between 0.5 to 5.0 km. (iv) Dust layers showed a complicated vertical structure and dust was

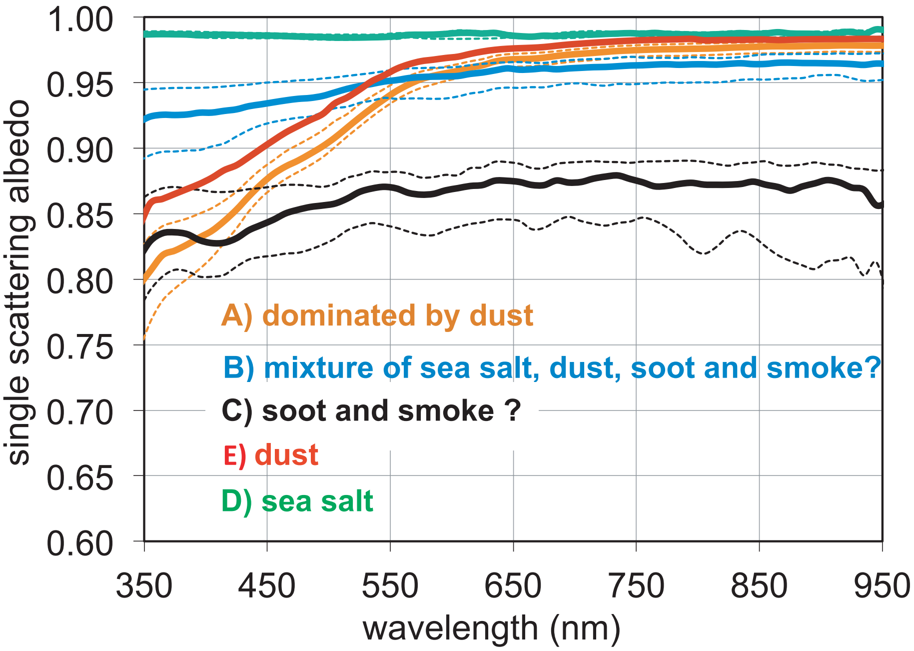

Fig. 4. Spectral single scattering albedos derived from SOAP. Shown are the median and the 25th and 75th percentile values for each period according to the classification.

mixed many times down into the marine surface layer. Results of Knippertz et al. (2011) are in agreement with findings of our study.

5.3. *Imaginary parts of refractive indices*

Schladitz et al. (2011b) showed that Mie theory is not appropriate for calculating scattering coefficients for non-spherical mineral dust particles. It is also shown that spherical Mie theory is applicable for periods with low dust concentrations, what gives confidence that measurements of particle number size distribution and scattering coefficients are consistent among each other. For the retrieval of the imaginary parts of refractive indices, the spherical Mie theory can be applied, since the particle absorption is less sensitive to particle shape Kalashnikova and Sokolik (2004).

Imaginary parts of refractive indices were derived by inverse Mie calculations using the measured particle number size distributions and absorption coefficients. The real part of refractive index of 1.53 for mineral dust was taken from the OPAC (Optical properties of Aerosols and Clouds) database (Hess et al., 1998). Also during SAMUM-1 real parts of 1.53 were derived in Schalditz et al. (2009), and in Kandler et al. (2011a,b) real parts between 1.55 and 1.58 were derived for the SAMUM-2 campaign. Differences between these values are small, and had no effect on the following method for retrieving the imaginary part of refractive indices.

The imaginary part of refractive index was varied, until the calculated absorption fitted to the measured absorption coefficient. Atmospheric aerosols are typically a mixture of several modes of particles with each mode having different chemical composition. Beside these facts, particles of a certain size may consist of only a single compound (external mixture) or multiple compounds (internal mixture). The Mie model used here assumes a size-independent refractive index with a homogeneous internal mixture of different compounds. Thus, the imaginary parts of refractive indices inferred by this method have to be regarded as effective values for the entire particle population.

The measurement uncertainty of the imaginary part of refractive index depends on the uncertainties of measuring the absorption coefficient and the particle number size distribution.

The uncertainty in the absorption is 15% and the uncertainty of the particle number size distribution was assumed to be 20%, what is the value of the uncertainty of the total mass concentration determined from the particle number size distribution (Schladitz et al. 2011a). In a first approximation, the imaginary part of refractive indices is a linear function of both, the particle mass concentration and the absorption coefficient, and thus, the uncertainty is the sum of both contributions and amounts about 35%.

Figure 5 shows imaginary parts of refractive indices determined for the entire time series for the wavelengths of 450, 550 and 650 nm. For the dust case, period E, the imaginary part of refractive indices is smaller than for other days, e.g. two days before the dust case (DOY 27 to 28). The highest total mass concentrations were measured during this period. A possible explanation might be that additional absorbers such as soot or biomass burning smoke could increase the imaginary part of

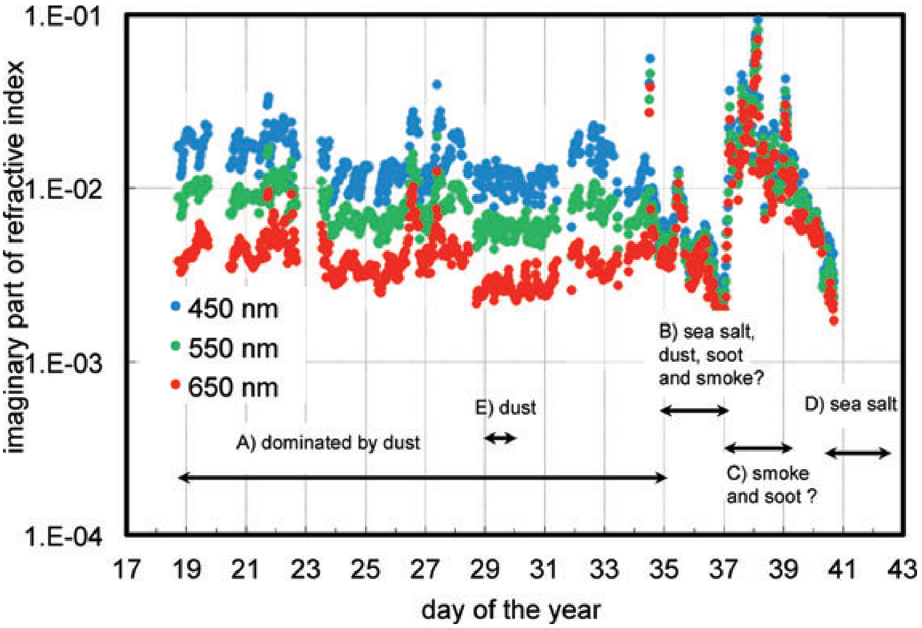

Fig. 5. Time series of the imaginary part of refractive index at 450, 550 and 650 nm. Also periods according the classification are shown.

refractive indices during other periods. Such events might occur at DOY 26.5, 27.5, 34.5 and 38. For these cases, it is difficult to distinguish between absorption of mineral dust, soot, and biomass burning smoke. Engelmann et al. (2011) reported smoke layers and possible down mixing of smoke to the ground. But differences in the spectral absorption between biomass burning smoke, soot (Kirchstetter et al., 2004) and mineral dust (Müller et al., 2009a) might be too small to allow a separation of compounds in such a complex mixture.

During Period B the imaginary part of refractive index showed only small wavelength dependence, which justifies the assumption that this period was dominated by many compounds with varying mass concentration over time. During period C, the imaginary part of refractive index was similar for all wavelengths. That indicates that mineral dust can be neglected, and that high imaginary parts of refractive indices were caused by soot or smoke or a mixture of both compounds. Period D was similar to period B, but with a higher sea salt mass concentration.

For the Periods A, B, C and E, imaginary parts of refractive indices were derived for wavelengths from 350 to 950 nm and are shown in Fig. 6. Median values for a dust case (periode E) and for the entire campaign are given in Table 1. For period A, the spectral imaginary parts of refractive indices show the typical spectral behaviour for mineral dust. The imaginary part for mineral dust is lowest with values smaller 4×10^{-3} in the wavelength range from 600 to 900 nm, and for wavelengths smaller 600 nm the imaginary part of refractive index increases with decreasing wavelength.

Spectra for the dust dominated case and the case with high dust concentration show a similar behaviour. While the values of the imaginary parts of refractive index are similar for smaller wavelengths, the dust case shows smaller imaginary parts of refractive index in the visible and NIR spectral range. This might be an indication that the other cases were ‘contaminated’ with another spectral neutral absorber. The imaginary part of the refractive index for period B is less dependent on wavelength. Only a small increase to smaller wavelength can be seen. Period C shows a similar spectral dependence, but with almost an order of magnitude higher values. The absorption Ångström exponent for period C is 1.2. From this value, a mixing ratio between soot-like and smoke-like absorbers cannot be concluded. The imaginary part of refractive index of pure soot given in the OPAC database shows a small increase towards smaller wavelengths. For 900 and 350 nm, the imaginary parts of refractive indices are 0.437 and, 0.465, respectively. Values for refractive indices given in literature can differ among each other. More references for wavelength dependence refractive indices are for example, Chang and Charalampopoulos (1990) and Bergstrom et al. (2002). The values derived for the total aerosol for period C were significantly smaller due to a mixing with non-absorbing material and were 0.035 and 0.014 for the wavelength 350 and 900, respectively. It is not clear if the stronger spectral dependence is due to absorbing organic compounds or due the simplified Mie model with a size-independent complex refractive index. Thus, the spectral behaviour shown in Fig. 6 is not an indication for a smoke-like absorber. The increasing imaginary part of refractive index with decreasing wavelengths might be also an artefact of the model or might be caused by systematic errors of the measurements. Periods A and D are dominated by sea salt and mineral dust and the total particle volume concentration is dominated by particles in the coarse mode. Thus, the Mie inversion routine retrieves

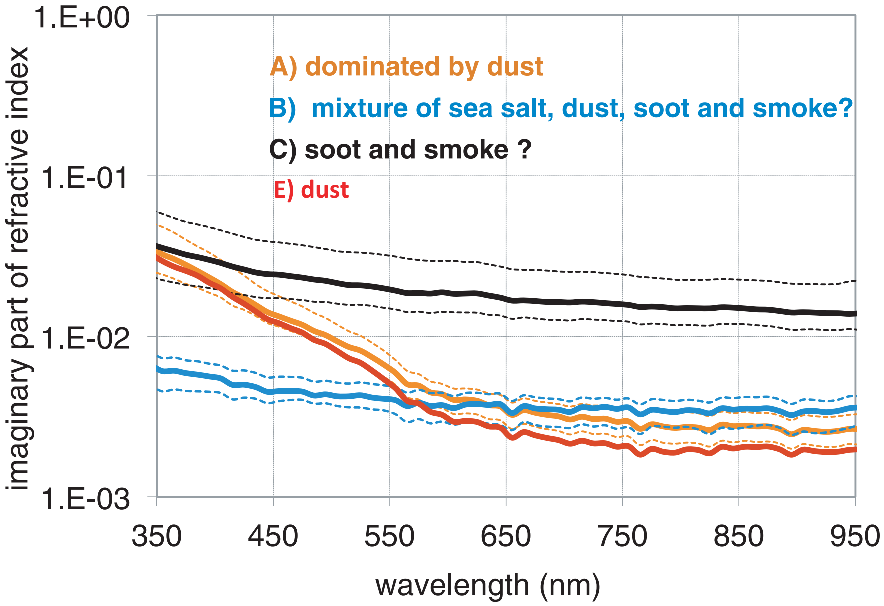

Fig. 6. Spectral imaginary parts of refractive indices. Shown are the median and variability within the period given by the 25th and 75th percentiles.

Table 1. *Median values of imaginary parts of refractive indices (k) for a dust case and the entire campaign*

Wavelength (nm)	320	350	400	450	500	550	600	650	750	850	950
Dust case (period E)	35.3	31.2	19.3	11.0	7.6	4.8	3	2.5	2.1	2	1.8
Median of the entire campaign	27.1	23.4	16.0	10.4	8.0	5.7	4.4	3.9	3.6	3.6	3.6

Note: Values for imaginary parts are given in k × 1000.

imaginary parts of refractive indices for coarse mode particles without significant uncertainties due to the assumption of size-independent imaginary parts of refractive indices. Potential uncertainties due to the assumption of an internal mixture still remain.

In Kandler et al. (2011a,b), the complex refractive index of particles was derived from the elemental composition measured with electron microscopy and coupled X-ray fluorescence detection. The refractive index was calculated by modelling the measured elemental composition by a set of mineralogical compounds and afterwards applying a volume mixture rule to average tabulated refractive index values for the identified minerals, according to their volume contribution to each single particle. For each size interval, the volume-weighted averages were calculated. A grand volume average was determined by weighting with the particle number size distributions measured downstream of the PM_{10} inlet. For electron microscopy the uncertainty in the imaginary part of refractive index was determined to be a factor between 2 (coarse mode particles) and 3 (submicrometer particles; Kandler et al., 2011a). For further analysis, an average uncertainty of 2.5 was used. Figure 7 shows imaginary parts of refractive indices derived by electron microscopy and by absorption spectroscopy.

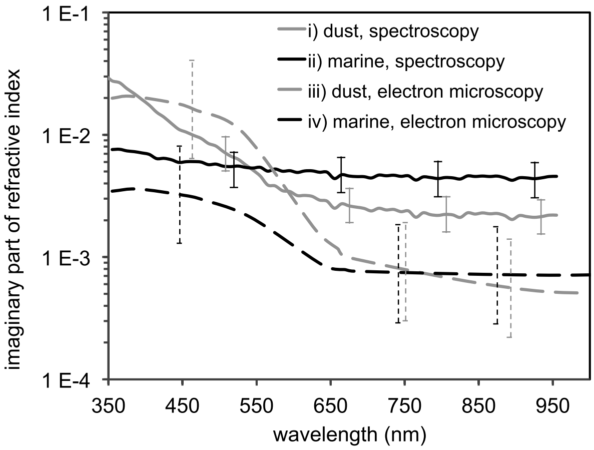

Fig. 7. Imaginary parts of refractive indices for dust and marine periods derived from this study and by electron microscopy (Kandler et al. 2011a,b). For the description of the dust and marine phases refer to text.

Two different types of aerosols, marine and mineral dust, were investigated. In the rest of this paragraph the classification according to Kandler et al. (2011a) is used. The cases classified as 'marine' in Kandler et al. (2009) coincide with periods

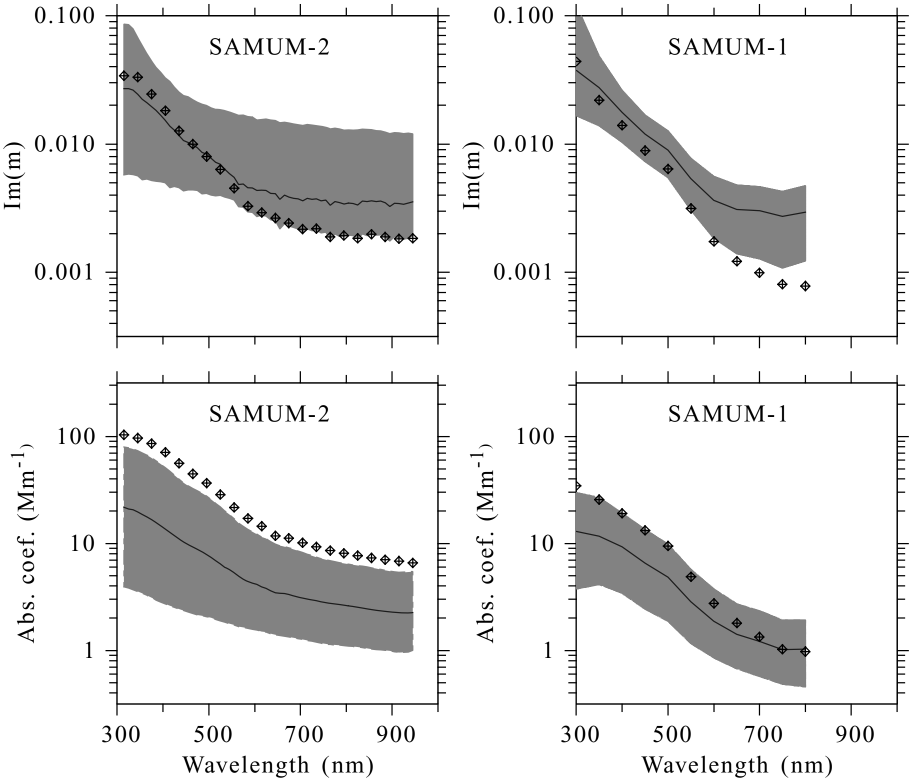

Fig. 8. Measured Absorption coefficients and derived imaginary parts of refractive indices for SAMUM-1 and SAMUM-2. Shown are the medians (lines), 10th and 90th percentiles (shaded area) of the entire campaigns. Also typical dust cases (diamonds) are shown, which are not necessarily periods with the highest dust concentrations.

classified as 'sea salt' in this manuscript. Imaginary parts of refractive indices denoted as 'dust' were determined by electron microscopy for the periods 29 January 11:37–11:48 and 19:23–19:33, 30 January 15:53–16:03 and 19:17–19:28, and 31 January 10:45–11:38 and by the absorption spectroscopy as an hourly average starting at 29 January 12:00 and 19:00, 30 January 16:00 and 19:00, and 31 January 11:00. For the marine case, data from different time periods had to be used for the two methods, because no period was found for which data from both measurement techniques are available. For the electron microscopy measurement, the periods 15 January 16:43–18:43 and 16 January 16:52–17:51 were used. For absorption spectroscopy the averaging period was from 29 January 00:00 to 23:00.

For the dust case, the imaginary parts of refractive indices at wavelengths larger than 550 nm determined by absorption spectroscopy are higher than values inferred from electron microscopy. In the wavelength range from 450 to 600 nm differences between these methods are small. For the marine case, the imaginary parts of refractive indices show a spectral run which is different to the dust cases. The flat spectral run indicates that a significant part of absorption comes from elemental carbon with absorption Ångström exponents in the order of unity. In the marine case, the values derived by electron microscopy are generally lower than values from absorption spectroscopy. Due to the high uncertainties the curves are only non-significantly different for the dust case. Only a further reduction of these uncertainties might reveal systematic differences between the methods and should be addressed in future work.

The differences between the two methods have to be explained by a set of uncertainties inherent to both methods. Values derived by absorption spectroscopy might by erroneous, because the imaginary part of refractive index is determined with Mie scattering calculations, possibly inaccurate for non-spherical dust particles. A further source of errors might be sizing with DMPS and APS, which requires a number of corrections. Refractive indices derived by electron microscopy have to rely on refractive index values tabulated in literature for pure minerals, which were measured with very different methods. In addition, the state of iron in the samples, the main factor influencing the mineral dust absorption, is not well known (Kandler et al., 2009). In addition, small soot inclusions in larger particles like sea salt would be disregarded by the analysis, but still may contribute to the absorption. Also, the calculation procedure depends on the choice of an adequate mixing rule for refractive indices reflecting the particle geometry, but the internal structure of the particles is largely unknown. For the marine case, data from different time periods had to be used for the two methods, what prohibits comparison in a strict sense.

5.4. Comparison with results of SAMUM-1

Absorption coefficients and imaginary parts of refractive indices inferred from SAMUM-1 and SAMUM-2 were compared. In Fig. 8, spectra of the median absorption coefficients and imaginary parts of refractive indices are shown. The variation during the campaigns is indicated by the 10th and 90th percentiles. In addition, for both campaigns 'mineral dust' spectra are given. For SAMUM-1, a period with high dust concentration was taken and an additional contribution of soot to absorption coefficients and imaginary parts of refractive indices was corrected for (Müller et al., 2009a). For SAMUM-2, period E is taken as dust case. A correction of the soot contributions was not done. The field station at Praia was far from anthropogenic sources considering the wind direction. Thus, an aerosol with a complex mixture of mineral dust, sea salt, marine particles and soot was expected. The complex mixtures prevented a correction for soot, to derive the spectra of pure mineral dust.

Absorption coefficients show a similar behaviour for SAMUM-1 and SAMUM-2. The median absorption coefficient of the entire campaign is higher for SAMUM-2. On a first sight, this is confusing, since SAMUM-1 took place in a source region of mineral dust, the dust measured during SAMUM-2 was transported of long distances to the Cape Verde Islands. Almost two-third of the measurements during SAMUM-2 campaign were however classified as dust dominated and many days without any significant amount of dust occurred during SAMUM-1. For SAMUM-1, not all data for cases with very high dust concentrations were available, since the SOAP filter were overloaded preventing data evaluation for these cases. Thus, many interruptions of the SAMUM-1 time series at high dust concentrations cause a bias. For this reason, the absorption spectrum for SAMUM-1 showed much smaller values than for SAMUM-2.

Imaginary parts of refractive indices show similar values for wavelengths smaller than 500 nm. For larger wavelengths, values inferred from SAMUM-2 are higher. The reader should remind that the SAMUM-1 experiment held in southern Morocco was an experiment in a source region with a minimum impact of marine, anthropogenic, and biogenic aerosol sources. In Müller et al. (2009a) it was shown that even small amounts of soot can change the derived imaginary part of refractive index in the wavelength range from 500 to 900 nm. The median and percentiles of the entire campaign show that the variability of imaginary parts was more variable during SAMUM-2 compared to SAMUM-1. The higher variability is explained by the complex mixing state during SAMUM-1.

6. Conclusions

We presented an improved SOAP. Beside the technical modifications concerning spectral range and resolution the data evaluation scheme was improved as well. Measuring transmittance and reflectance gives information on the particle scattering. It was shown that a calibration using a nephelometer as a reference instrument, particle scattering coefficients can be derived from SOAP.

From measurements with the SOAP and the integrating nephelometer, absorption and scattering Ångström exponents, and the spectral single scattering albedo of different aerosol types were derived. Comparison with columnar integrated measurements showed, that single scattering albedos compared well for a dust case (Toledano et al., 2011).

Measurements of basic aerosol parameters were used for a classification of aerosol types by their optical properties. The classification was based on a small set of instruments with only physical measurements of the scattering and absorption coefficients, and number size distributions. The derivation does not include a chemical or elemental analysis. Five periods were found with different optical properties. These are dust periods for about 16 days, periods with complex mixtures of mineral dust, sea salt, soot and marine background aerosols. From optical properties a down mixing of smoke can be neither affirmed nor excluded. A quantification of single compounds was not possible, since the state of mixing was too complex to give a unique solution.

Imaginary parts of refractive indices show different spectral behaviours for cases with high dust concentrations and cases with marine background aerosol. For dust cases, imaginary parts of refractive indices range from 0.020 at 400 nm to 0.0018 at 950 nm. For the entire campaign, median values range from 0.016 at 400 nm to 0.0035 at 950 nm. Spectral imaginary parts of refractive indices for mineral dust were similar to values measured during SAMUM-2. Comparison with values inferred from electron microscopy shows that there are still uncertainties between these methods.

From in situ measurements of optical properties, we cannot conclude significant aging effects of mineral dust particles during transport from the Saharan to the Cape Verde Islands.

7. Acknowledgments

This study was supported by the German Research Foundation under grant MU 2669/1–1 and grant FOR 539 in the framework of the research group SAMUM.

References

Anderson, T. L., Covert, D. S., Marshall, S. F., Laucks, M. L., Charlson, R. J., and co-authors. 1996. Performance characteristics of a high-sensitivity, three-wavelength, total scatter/backscatter nephelometer. *J. Atmos. Oceanic Technol.* **13**, 967–986.

Anderson, T. L. and Ogren, J. A. 1998. Determining aerosol radiative properties using the TSI 3563 integrating nephelometer. *Aerosol Sci. Tech.* **29**, 57–69.

Ångström, A. 1929. On the atmospheric transmission of Sun radiation and on dust in the air. *Geogr. Anal.* **12**, 155–156.

Ansmann, A., Petzold, A., Kandler, K., Tegen, I., Wendisch, M., and co-authors. 2011. Saharan Mineral Dust Experiments SAMUM-1 and SAMUM-2: What have we learned? *Tellus* **63B**, this issue.

Arnott, W. P., Hamasha, K., Moosmüller, H., Sheridan, P. J. and Ogren, J. A. 2005. Towards aerosol light-absorption measurements with a 7-wavelength Aethalometer: evaluation with a photoacoustic instrument and 3-wavelength nephelometer. *Aerosol Sci. Tech.* **39**, 17–29.

Bergstrom, R. W., Russell, P. B. and Hignett, P. 2002. Wavelength dependence of the absorption of black carbon particles: predictions and results from the TARFOX experiment and implications for the aerosol single scattering albedo. *J. Atmos. Sci.* **59**, 567–577.

Birmili, W., Stratmann, F. and Wiedensohler, A. 1999. Design of a DMA-based size spectrometer for a large particle size range and stable operation. *J. Aerosol Sci.* **30**, 549–553.

Birmili, W., Schepanski, K., Ansmann, A., Spindler, G., Tegen, I., and co-authors. 2008. A case of extreme particulate matter concentrations over Central Europe caused by dust emitted over the southern Ukraine. *Atmos. Chem. Phys.* **8**, 997–1016.

Bohren, C. F. 1987. Multiple-scattering of light and some of its observable consequences. *Am. J. Phys.* **55**, 524–533.

Bond, T. C., T. L. Anderson, et al. 1999. Calibration and intercomparison of filter-based measurements of visible light absorption by aerosols. *Aerosol Science and Technology* **30**, 582–600.

Brockmann, J. E. 1993. Sampling and Transport of Aerosols. In: *Aerosol Measurement – Principles, Techniques, and Applications* (eds. K. Willeke and P. A. Baron). Van Nostrand Reinhold, New York, 77–108.

Chang, H. and Charalampopoulos, T. T. 1990. Determination of the wavelength dependence of refractive indices of flame soot. *P. Roy. Soc. Lond. A Math. Phys. Sci.* **430**, 577–591.

Coen, M. C., Weingartner, E., Schaub, D., Hueglin, C., Corrigan, C., and co-authors. 2004. Saharan dust events at the Jungfraujoch: detection by wavelength dependence of the single scattering albedo and first climatology analysis. *Atmos. Chem. Phys* **4**, 2465–2480.

DeCarlo, P., Slowik, J., Worsnop, D., Davidovits, P. and Jimenez, J. 2004. Particle morphology and density characterization by combined mobility and aerodynamic diameter measurements. Part 1: Theory. *Aerosol Sci. Tech.* 38, 1185–1205.

Engelmann, R., Ansmann, A., Horn, S., Seifert, P., Althausen, D., and co-authors. Doppler lidar studies of heat island effects on vertical mixing of aerosols during SAMUM-2. *Tellus* **63B**, this issue.

Fialho, P., Freitas, M. C., Barata, F., Vieira, B., Hansen, A. D. A., and co-authors. 2006. The Aethalometer calibration and determination of iron concentration in dust aerosols. *J. Aerosol Sci.* **37**, 1497–1506.

Haywood, J.M. and Bougher, O. 2000. Estimates of the direct and indirect radiative forcing due to tropospheric aerosols: a review. *Rev. Geophys.* **38**, 513–543.

Haywood, J. M., Francis, P. N., Glew, M. D. and Taylor, J. P. 2001. Optical properties and direct radiative effect of Saharan dust- a case study of two Saharan dust outbreaks using aircraft data. *J. Geophys. Res.* **106**(D16), 18 417–18 430.

Haywood, J.M., Francis, P., Osborne, S., Glew,M., Loeb, N., and co-authors. 2003. Radiative properties and direct radiative effect of saharan dust measured by the c-130 aircraft during SHADE: 1. Solar spectrum. *J. Geophys. Res.* **108**(D18), 8577, doi:10.1029/2002JD002687.

Heinold, B., Tegen, I., Schepanski, K. and Hellmuth, O. 2008. Dust radiative feedback on Saharan boundary layer dynamics and dust mobilization. *Geophys. Res. Lett.* **35**, doi:09810.01029/02008GL033654.

Heinold, B., Tegen, I., Esselborn, M., Kandler, K., Knippertz, P., and co-authors. 2009. Regional Saharan dust modelling during the SAMUM 2006 campaign. *Tellus* **61B**, 307–324.

Heintzenberg, J., Charlson, R. J., Clarke, A. D., Liousse, C., Ramaswamy, C. V., and co-authors. 1997. Measurements and modelling of aerosol single-scattering albedo: progress, problems and prospects. *Contrib. Atmos. Phys.* **70**, 249–264.

Heintzenberg, J., Wiedensohler, A., Tuch, T. M., Covert, D. S., Sheridan, P., and co-authors. 2006. Intercomparisons and aerosol calibrations of 12 commercial integrating nephelometers of three manufacturers. *J. Atmos. Oceanic Technol.* **23**, 902–914.

Heintzenberg, J. 2009. The SAMUM-1 experiment over Southern Morocco: overview and introduction. *Tellus* **61B**, 2–11.

Hess, M., Koepke, P. and Schult, I. 1998. Optical properties of aerosols and clouds: the software package OPAC. *B. Am. Meteorol. Soc.* **79**, 831–844.

IPCC, 2007. Climate change 2007. The physical science basis. In: *Contribution of Working Group 1 to the Fourth Assessment Report of the Intergovernmental Panel on Climate Change (IPCC)* (eds. A. S. Solomon, D. Qin, M. Manning, M. Marquis, K. Averyt and co-editors). Cambridge University Press, Cambridge, United Kingdom and New York, NY, USA.

Kahn, R. A., Petzold, A.,Wendisch, M., Bierwirth, E., Dinter, T., and co-authors. 2009. Desert dust aerosol mass mapping in the western Sahara, using particle properties derived from space-based multi-angle imaging. *Tellus* **61B**, 239–251.

Kalashnikova, O. V. and Sokolik, I. N. 2004. Modeling the radiative properties of nonspherical soil-derived mineral aerosols, *J. Quant. Spectrosc. Radiat. Transfer*, **87**, 137–166.

Kandler, K., Schütz, L., Deutscher, C., Ebert, M., Hofmann, H., and co-authors. 2009. Size distribution, mass concentration, chemical and mineralogical composition and derived optical parameters of the boundary layer aerosol at Tinfou, Morocco, during SAMUM 2006. *Tellus* **61B**, 32–50.

Kandler, K., Lieke, K., Benker, N., Emmel, C., Küpper, M., and co-authors. 2011a. Electron microscopy of particles collected at Praia, Cape Verde, during the Saharan Mineral Dust Experiment: particle chemistry, shape, mixing state and complex refractive index. *Tellus* **63B**, this issue.

Kandler, K., Schütz, L., Jäckel, S., Lieke, K., Emmel, C., and co-authors. 2011b. Ground-based off-line aerosol measurements at Praia, Cape Verde, during the Saharan Mineral Dust Experiment: microphysical properties and mineralogy. *Tellus* **63B**, this issue.

Kaufman, Y. J., Koren, I., Remer, L. A., Tanre, D., Ginoux, P., and co-authors. 2005. Dust transport and deposition observed from the Terra-Moderate Resolution Imaging Spectroradiometer (MODIS) spacecraft over the Atlantic ocean. *J. Geophys. Res.-Atmos.* **110**, doi:10.1029/2003JD004436.

Kirchstetter, T. W., Novakov, T. and Hobbs, P. V. 2004. Evidence that the spectral dependence of light absorption by aerosols is affected by organic carbon. *J. Geophys. Res.-Atmos.* **109**, doi:10.1029/2004JD004999.

Knippertz, P., Tesche, M., Heinold, B., Kandler, K., Toledano, C., and co-authors. 2011. Dust Mobilization and Aerosol Transport from West

Africa to Cape Verde: a meteorological overview of SAMUM-2. *Tellus* **63B**, this issue.

Linke, C., Möhler, O., Veres, A., Mohacsi, A., Bozoki, Z., and co-authors. 2006. Optical properties and mineralogical composition of different Saharan mineral dust samples: a laboratory study. *Atmos. Chem. and Phys.* **6**, 3315–3323.

Meusinger, C. 2009. Calibration of a spectral particle absorption photometer for determination of atmospheric mineral dust concentrations and measurements on Cape Verde Islands. *Master Thesis*, University Leipzig.

Mishchenko, M. I., Lacis, A. A., Carlson, B. E. and Travis, L. D. 1995. Nonsphericity of dust-like tropospheric aerosols – implications for aerosol remote-sensing and climate modeling. *Geophys. Res. Lett.* **22**, 1077–1080.

Müller, T., Schladitz, A., Massling, A., Kaaden, N., Kandler, K., and co-authors. 2009a. Spectral absorption coefficients and imaginary parts of refractive indices of Saharan dust during SAMUM-1. *Tellus* **61B**, 79–95.

Müller, D., Heinold, B., Tesche, M., Tegen, I., Althausen, D., and co-authors. 2009b. EARLINET observations of the 14–22 May long-range dust transport event during SAMUM 2006: validation of results from dust transport modelling. *Tellus* **61B**, 325–339.

Müller, T., Nowak, A., Wiedensohler, A., Sheridan, P., Laborde, M., and co-authors. 2009c. Angular illumination and truncation of three different integrating nephelometers: implications for empirical, size-based corrections. *Aerosol Sci. Tech.* **43**, 581–586.

Müller, T., J. S. Henzing, et al. 2011. Characterization and intercomparison of aerosol absorption photometers: result of two intercomparison workshops. *Atmospheric Measurement Techniques* **4**, 245–268.

Petzold, A., Rasp, K., Weinzierl, B., Esselborn, M., Hamburger, T., and co-authors. 2009. Saharan dust absorption and refractive index from aircraft-based observations during SAMUM 2006. *Tellus* **61B**, 118–130.

Posfai, M., Anderson, J. R., Buseck, P. R. and Sievering, H. 1999. Soot and sulfate aerosol particles in the remote marine troposphere. *J. Geophys. Res.-Atmos.* 104, 21685–21693.

Prospero, J. M., Ginoux, P., Torres, O., Nicholson, S. E. and Gill T. E. 2002. Environmental characterization of global sources of atmospheric soil dust identification with the Nimbus 7 Total Ozone Mapping Spectrometer (TOMS) absorbing aeroso product. *Rev. Geophys.* **40**, doi:10.1029/2000RG000095.

Schladitz, A., Müller, T., Kaaden, N., Massling, A., Kandler, K., and co-authors. 2009. In situ measurements of optical properties at Tinfou (Morocco) during the Saharan Mineral Dust Experiment SAMUM 2006. *Tellus* **61B**, 64–78.

Schladitz, A., Müller, T., Nowak, A., Kandler, K., Lieke, K., and co-authors. 2011a. In-situ aerosol characterization at Cape Verde. Part 1: Particle number size distributions, hygroscopic growth and state of mixing of the marine and Saharan dust aerosol. *Tellus* **63B**, this issue.

Schladitz, A., Müller, T., Nordmann, S., Tesche, T., Groß, S., and co-authors. 2011b. In-situ aerosol characterization at Cape Verde. Part 2: parameterization of relative humidity- and wavelength-dependent aerosol optical properties. *Tellus* **63B**, this issue.

Sokolik, I. N. and Toon, O. B. 1996. Direct radiative forcing by anthropogenic airborne mineral aerosols. *Nature* **381**, 681–683.

Sokolik, I. N. and Toon, O. B. 1999. Incorporation of mineralogical composition into models of the radiative properties of mineral aerosol from UV to IR wavelengths. *J. Geophys. Res.-Atmos.* **104**, 9423–9444.

Tegen, I., Lacis, A. A. and Fung, I. 1996. The influence on climate forcing of mineral aerosols from disturbed soils. *Nature* **380**, 419–422.

Toledano, C., Wiegner, M., Groß, S., Freudenthaler, V., Gasteiger, J., and co-authors. 2011. Optical properties of aerosol mixtures derived from sun-sky radiometry during SAMUM-2, *Tellus* **63B**, this issue.

Tuch, T. M., Haudek, A., Müller, T., Nowak, A., Wex, H., and co-authors. 2009. Design and performance of an automatic regenerating adsorption aerosol dryer for continuous operation at monitoring sites. *Atmos. Meas. Tech.*, **2**, 417–422.